

# Intrinsic room-temperature piezoelectric quantum anomalous hall insulator in Janus monolayer $\text{Fe}_2\text{IX}$ ( $\text{X}=\text{Cl}$ and $\text{Br}$ )

San-Dong Guo<sup>1</sup>, Wen-Qi Mu<sup>1</sup>, Xiang-Bo Xiao<sup>2,3</sup> and Bang-Gui Liu<sup>2,3</sup>

<sup>1</sup>*School of Electronic Engineering, Xi'an University of Posts and Telecommunications, Xi'an 710121, China*

<sup>2</sup>*Beijing National Laboratory for Condensed Matter Physics, Institute of Physics, Chinese Academy of Sciences, Beijing 100190, People's Republic of China and*

<sup>3</sup>*School of Physical Sciences, University of Chinese Academy of Sciences, Beijing 100190, People's Republic of China*

A two-dimensional (2D) material with piezoelectricity, topological and ferromagnetic (FM) orders, namely 2D piezoelectric quantum anomalous hall insulator (PQAH), may open new opportunities to realize novel physics and applications. Here, by first-principles calculations, a family of 2D Janus monolayer  $\text{Fe}_2\text{IX}$  ( $\text{X}=\text{Cl}$  and  $\text{Br}$ ) with dynamic, mechanical and thermal stabilities is predicted to be room-temperature PQAH. At the absence of spin-orbit coupling (SOC), monolayer  $\text{Fe}_2\text{IX}$  ( $\text{X}=\text{Cl}$  and  $\text{Br}$ ) is a half Dirac semimetal state. When the SOC is included, these monolayers become quantum anomalous hall (QAH) states with sizable gaps (more than two hundred meV) and two chiral edge modes (Chern number  $C=2$ ). It is also found that monolayer  $\text{Fe}_2\text{IX}$  ( $\text{X}=\text{Cl}$  and  $\text{Br}$ ) possesses robust QAH states against biaxial strain. By symmetry analysis, it is found that only out-of-plane piezoelectric response can be induced by a uniaxial strain in the basal plane. The calculated out-of-plane  $d_{31}$  of  $\text{Fe}_2\text{ICl}$  ( $\text{Fe}_2\text{IBr}$ ) is 0.467 pm/V (0.384 pm/V), which is higher than or comparable with ones of other 2D known materials. Meanwhile, using Monte Carlo (MC) simulations, the Curie temperature  $T_C$  is estimated to be 429/403 K for monolayer  $\text{Fe}_2\text{ICl}/\text{Fe}_2\text{IBr}$  at FM ground state, which is above room temperature. Finally, the interplay of electronic correlations with nontrivial band topology is studied to confirm the robustness of QAH state. The combination of piezoelectricity, topological and FM orders makes monolayer  $\text{Fe}_2\text{IX}$  ( $\text{X}=\text{Cl}$  and  $\text{Br}$ ) become a potential platform for multi-functional spintronic applications with large gap and high  $T_C$ . Our works provide possibility to use the piezotronic effect to control QAH effects, and can stimulate further experimental works.

PACS numbers: 71.20.-b, 77.65.-j, 72.15.Jf, 78.67.-n

Email:sandongyuwang@163.com

Keywords: Ferromagnetism, Piezoelectronics, Topological insulator, Janus monolayer

## I. INTRODUCTION

Seeking 2D multifunctional piezoelectric materials is a compelling problem of novel physics and materials science<sup>1</sup>, like the combination of piezoelectricity with topological insulating phase, intrinsic ferromagnetism and quantum spin hall effect. Using piezoelectric effect to control the quantum or spin transport process may lead to novel device applications or scientific breakthroughs. Both in experiment and in theory, the advances have been made on 2D piezoelectric materials. Experimentally, the piezoelectricity has been reported in monolayer  $\text{MoS}_2$ ,  $\text{MoSSe}$  and  $\text{In}_2\text{Se}_3$ <sup>2-5</sup>. The piezoelectric properties of many 2D materials without inversion symmetry have been investigated by density functional theory (DFT) calculations, including strain-tuned effects on piezoelectricity<sup>6-15</sup>. Recently, some progress have been made on 2D multifunctional piezoelectric materials. The coexistence of intrinsic piezoelectricity and ferromagnetism, namely piezoelectric ferromagnetism (PFM), has been predicted in 2D vanadium dichalcogenides,  $\text{VSi}_2\text{P}_4$ ,  $\text{CrBr}_{1.5}\text{I}_{1.5}$  and  $\text{InCrTe}_3$ <sup>16-19</sup>. The combination of piezoelectricity with topological insulating phase has also been achieved in monolayer  $\text{InXO}$  ( $\text{X}=\text{Se}$  and  $\text{Te}$ )<sup>20</sup> and Janus monolayer  $\text{SrAlGaSe}_4$ <sup>21</sup>. A natural idea is to search for PQAH with piezoelectricity, topological and FM orders.

Many kinds of 2D magnetic materials have been widely investigated<sup>22-28</sup>, and the monolayer  $\text{Cr}_2\text{Ge}_2\text{Te}_6$ ,

$\text{CrI}_3$ ,  $\text{VS}_2$  and  $\text{VSe}_2$  have been experimentally confirmed<sup>23,25,26</sup>. The combination of ferromagnetism with topological insulating phase will produce QAH insulator, which can be characterized by a nonzero Chern number, being in accordance with the number of edge states. The QAH insulator is first observed experimentally in thin films of Cr doped  $(\text{Bi}, \text{Sb})_2\text{Te}$  below 30 mK<sup>29</sup>. Although various theoretical predictions and the new synthetic methods have been proposed, a higher-temperature QAH insulator is still a challenge in experiment<sup>29,30</sup>. Recently, a robust QAH insulator  $\text{Fe}_2\text{I}_2$  monolayer is proposed with a topologically nontrivial band gap of 301 meV, a nonzero Chern number  $C=2$  and a high Curie temperature (about 400 K)<sup>31</sup>. The experimental feasibility and stability of  $\text{Fe}_2\text{I}_2$  monolayer have been proved by the cohesive energy, phonon spectra and ab initio molecular dynamics (AIMD) simulations. However,  $\text{Fe}_2\text{I}_2$  monolayer possesses no piezoelectricity due to inversion symmetry.

It's a natural idea to achieve PQAH, based on monolayer  $\text{Fe}_2\text{I}_2$ . It is noted that the monolayer  $\text{Fe}_2\text{I}_2$  has sandwiched I-Fe-I structure. Inspiring from the already synthesized Janus monolayer  $\text{MoSSe}$ <sup>32</sup>, constructed by replacing one of two S layers with Se atoms in  $\text{MoS}_2$  monolayer, it is possible to achieve Janus structure based on  $\text{Fe}_2\text{I}_2$  monolayer, and then produce piezoelectricity. In this work, Janus monolayer  $\text{Fe}_2\text{IX}$  ( $\text{X}=\text{Cl}$  and  $\text{Br}$ ) is constructed based on QAH insulator  $\text{Fe}_2\text{I}_2$  monolayer by

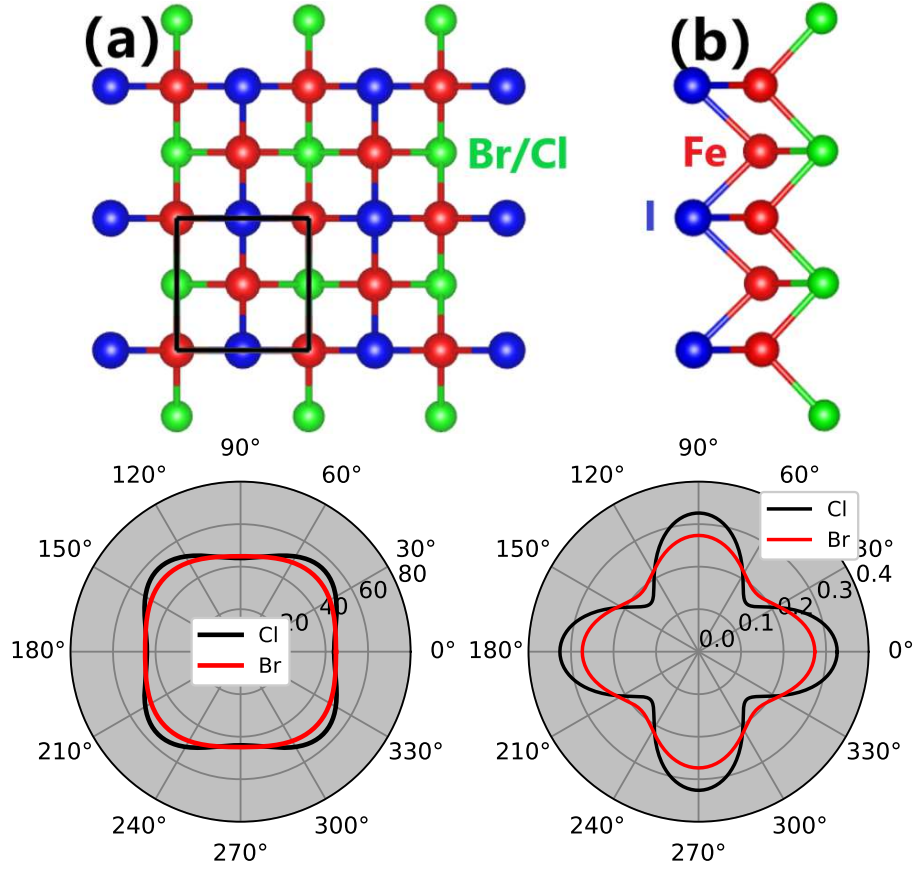


FIG. 1. (Color online) Top: the (a) top view and (b) side view of crystal structure of Janus monolayer  $\text{Fe}_2\text{IX}$  ( $\text{X}=\text{Cl}$  and  $\text{Br}$ ). The black frame represents the primitive cell. Bottom: the angular dependence of the Young's modulus ( $C_{2D}(\theta)$ ) and Poisson's ratio ( $\nu_{2D}(\theta)$ ) of Janus monolayer  $\text{Fe}_2\text{IX}$  ( $\text{X}=\text{Cl}$  and  $\text{Br}$ ).

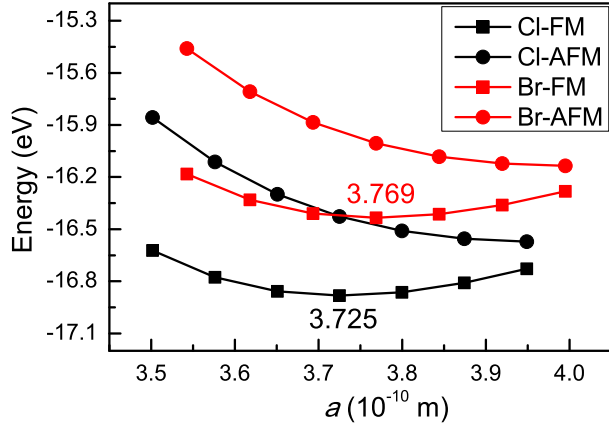


FIG. 2. (Color online) The FM and AFM energy of Janus monolayer  $\text{Fe}_2\text{IX}$  ( $\text{X}=\text{Cl}$  and  $\text{Br}$ ) as a function of lattice constants  $a$ .

replacing the top I atomic layer with X atoms. These Janus monolayers are dynamically, mechanically and thermally stable. By first-principles calculations, the nontrivial topological state of monolayer  $\text{Fe}_2\text{IX}$  ( $\text{X}=\text{Cl}$  and  $\text{Br}$ ) is

firmly confirmed by a nonzero Chern number ( $C=2$ ) and chiral edge states. Their nontrivial band gaps are larger than 200 meV, and the Curie temperatures are estimated to be about 400 K. By symmetry analysis, only out-of-plane piezoelectric response can be induced by a uniaxial strain, and the predicted out-of-plane  $d_{31}$  of  $\text{Fe}_2\text{ICl}$  ( $\text{Fe}_2\text{IBr}$ ) is 0.467 pm/V (0.384 pm/V), which is higher than or comparable with ones of other 2D known materials. These indicate the enormous potential of Janus monolayer  $\text{Fe}_2\text{IX}$  ( $\text{X}=\text{Cl}$  and  $\text{Br}$ ) in developing 2D piezoelectric spin topological devices.

The rest of the paper is organized as follows. In the next section, we shall give our computational details and methods. In the next few sections, we shall present crystal structure, structural stabilities, topological properties, piezoelectric properties and Curie temperatures of Janus monolayer  $\text{Fe}_2\text{IX}$  ( $\text{X}=\text{Cl}$  and  $\text{Br}$ ). Finally, we shall give our discussion and conclusions.

## II. COMPUTATIONAL DETAIL

First-principles calculations are carried out by DFT<sup>33</sup> using the VASP code<sup>34–36</sup>. The plane-wave basis with an

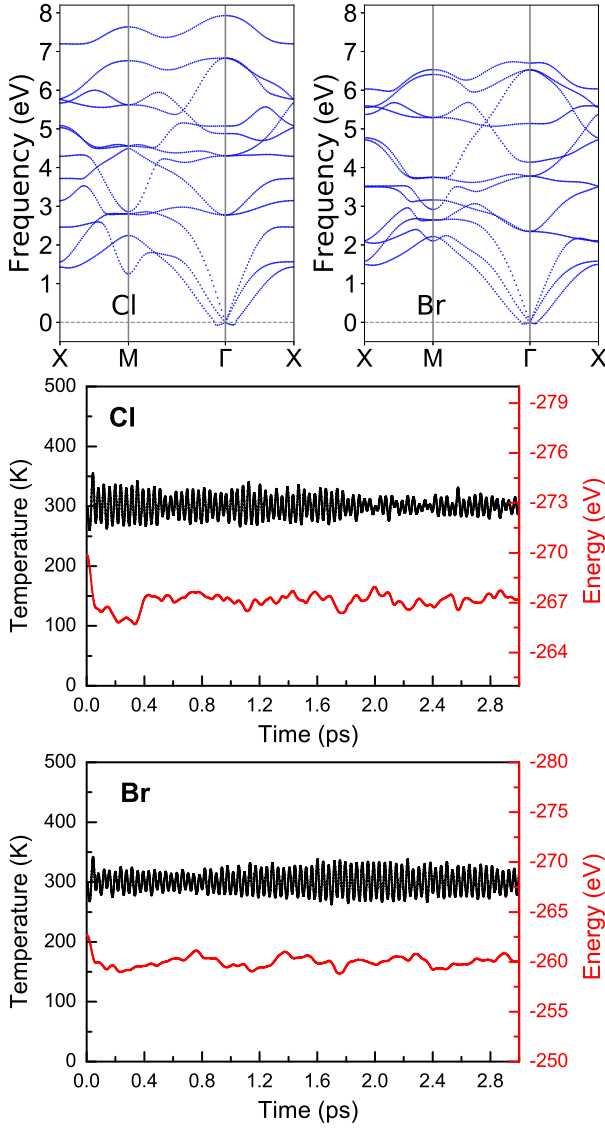


FIG. 3. (Color online) Top: the phonon band dispersions of Janus monolayer  $\text{Fe}_2\text{IX}$  ( $\text{X}=\text{Cl}$  and  $\text{Br}$ ) with FM magnetic configuration. Bottom: the temperature and total energy fluctuations of Janus monolayer  $\text{Fe}_2\text{IX}$  ( $\text{X}=\text{Cl}$  and  $\text{Br}$ ) with FM magnetic configuration at 300 K.

energy cutoff of 500 eV is used for Janus monolayer  $\text{Fe}_2\text{IX}$  ( $\text{X}=\text{Cl}$  and  $\text{Br}$ ). The exchange-correlation functional is approximated by the popular generalized gradient approximation (GGA) of Perdew, Burke and Ernzerhof<sup>37</sup>. The SOC is included in the calculations self-consistently. The total energy convergence criterion is set for  $10^{-8}$  eV. All the lattice constants and atomic coordinates are optimized with the force on each atom being less than  $0.0001 \text{ eV}\cdot\text{\AA}^{-1}$ . A vacuum spacing of more than  $15 \text{ \AA}$  is used to avoid artificial interactions caused by the periodic boundary condition. The DFT+ $U$  method<sup>38</sup> is employed for the treatment of the strongly correlated  $3d$  electrons of Fe atom with  $U_{\text{eff}} = 2.5 \text{ eV}$ <sup>31,39</sup> for studied monolayers.

The elastic stiffness tensor  $C_{ij}$  are carried out by using strain-stress relationship (SSR) with GGA, and the piezoelectric stress tensor  $e_{ij}$  are calculated by density functional perturbation theory (DFPT) method<sup>40</sup> using GGA+SOC. A Monkhorst-Pack k-mesh of  $18\times 18\times 1$  is used to sample the Brillouin Zone (BZ) for the self-consistent calculations and elastic coefficients  $C_{ij}$ . To attain the accurate  $e_{ij}$ , a dense mesh of  $26\times 26\times 1$  k-points is adopted. The 2D elastic coefficients  $C_{ij}^{2D}$  and piezoelectric stress coefficients  $e_{ij}^{2D}$  have been renormalized by  $C_{ij}^{2D} = Lz C_{ij}^{3D}$  and  $e_{ij}^{2D} = Lz e_{ij}^{3D}$ , where the  $Lz$  is the length of unit cell along  $z$  direction.

The interatomic force constants (IFCs) with the  $5\times 5\times 1$  supercell are obtained with FM ground state by finite displacement method. From calculated harmonic IFCs, the phonon dispersions are evaluated using Phonopy code<sup>41</sup>. Surface state and Berry curvature calculations are carried out by WannierTools code, based on the tight-binding Hamiltonians constructed from maximally localized Wannier functions by Wannier90 code<sup>42,43</sup>. The Curie temperature is estimated by MC simulation using Mcsolver code<sup>44</sup>.

### III. CRYSTAL STRUCTURE

Similar to monolayer  $\text{Fe}_2\text{I}_2$ <sup>31</sup>, Janus monolayer  $\text{Fe}_2\text{IX}$  ( $\text{X}=\text{Cl}$  and  $\text{Br}$ ) contains three atomic sublayers with Fe layer sandwiched between I and X layers, whose unit cell contains four atoms with two co-planar Fe atoms. The schematic crystal structures of Janus monolayer  $\text{Fe}_2\text{IX}$  ( $\text{X}=\text{Cl}$  and  $\text{Br}$ ) are shown in Figure 1. Similar to Janus monolayer MoSse from MoS<sub>2</sub><sup>32</sup>, the Janus monolayer  $\text{Fe}_2\text{IX}$  ( $\text{X}=\text{Cl}$  and  $\text{Br}$ ) can be constructed by replacing one of two I layers with X atoms in monolayer  $\text{Fe}_2\text{I}_2$ . Janus monolayer  $\text{Fe}_2\text{IX}$  ( $\text{X}=\text{Cl}$  and  $\text{Br}$ ) crystallizes in the orthorhombic  $P4mm$  space group (No.99), which loses centrosymmetry compared to centrosymmetric monolayer  $\text{Fe}_2\text{I}_2$  with  $P4/nmm$  space group (No. 129). The missing centrosymmetry will lead to piezoelectricity for Janus monolayer  $\text{Fe}_2\text{IX}$  ( $\text{X}=\text{Cl}$  and  $\text{Br}$ ).

To determine the ground state of  $\text{Fe}_2\text{IX}$  ( $\text{X}=\text{Cl}$  and  $\text{Br}$ ), two different initial magnetic configurations, including antiferromagnetic (AFM) and FM states, are used, and the energy of FM and AFM states as a function of lattice constants  $a$  are shown in Figure 2. It is clearly seen that the FM order is the most stable magnetic state for Janus monolayer  $\text{Fe}_2\text{IX}$  ( $\text{X}=\text{Cl}$  and  $\text{Br}$ ), which means that ferromagnetism in monolayer  $\text{Fe}_2\text{I}_2$  is retained by elements substitution engineering. The optimized lattice constants with FM state is  $3.725 \text{ \AA}$  for  $\text{Fe}_2\text{ICl}$ , and  $3.769 \text{ \AA}$  for  $\text{Fe}_2\text{IBr}$ . Due to different atomic sizes and electronegativities of Cl/Br and I atoms, the inequivalent Fe-Cl/Br and Fe-I bond lengths (Cl/Br-Fe-Cl/Br and I-Fe-I bond angles) from Table I can induce a built-in electric field. It is clearly seen that  $\text{Fe}_2\text{ICl}$  has greater deviation from horizontal mirror symmetry than  $\text{Fe}_2\text{IBr}$ .

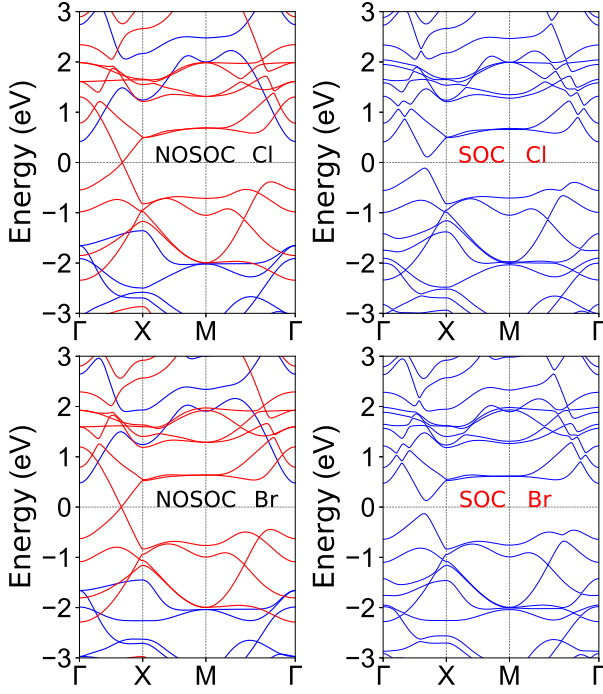


FIG. 4. (Color online) The energy band structures of Janus monolayer  $\text{Fe}_2\text{IX}$  ( $\text{X}=\text{Cl}$  and  $\text{Br}$ ) without and with SOC at the FM ground state. The blue (red) lines represent the band structure in the spin-up (spin-down) direction without SOC.

TABLE I. The structural parameters including lattice constants  $a_0$  (Å); Fe-Cl/Br ( $d_1$ ) and Fe-I ( $d_2$ ) bond lengths (Å); Cl/Br-Fe-Cl/Br ( $\theta_1$ ) and I-Fe-I ( $\theta_2$ ) angles; the thickness layer height ( $t$ ) (Å).

Name	$a_0$	$d_1$	$d_2$	$\theta_1$	$\theta_2$	$t$
$\text{Fe}_2\text{ICl}$	3.725	2.463	2.700	98.259	87.253	3.566
$\text{Fe}_2\text{IBr}$	3.769	2.582	2.704	93.747	88.355	3.704

#### IV. STRUCTURAL STABILITY

Figure 3 shows the the phonon spectra of Janus monolayer  $\text{Fe}_2\text{IX}$  ( $\text{X}=\text{Cl}$  and  $\text{Br}$ ), which can be used to analyze their dynamical stabilities. The nine optical and three acoustical phonon branches with a total of twelve branches due to four atoms per unitcell can be observed. Their phonon spectra show no imaginary frequency, which confirms the dynamical stability of monolayer  $\text{Fe}_2\text{IX}$  ( $\text{X}=\text{Cl}$  and  $\text{Br}$ ), and they can exist as free-standing 2D crystals. The thermal stability of the monolayer  $\text{Fe}_2\text{IX}$  ( $\text{X}=\text{Cl}$  and  $\text{Br}$ ) can be checked by AIMD simulations using NVT ensemble with a supercell of size  $4 \times 4 \times 1$  for more than 3000 fs with a time step of 1 fs. The temperature and total energy fluctuations of monolayer  $\text{Fe}_2\text{IX}$  ( $\text{X}=\text{Cl}$  and  $\text{Br}$ ) as a function of the simulation time are plotted in Figure 3 at room temperature. No obvious structural disruption is observed with small the temperature and total energy fluctuates, which con-

firms the thermodynamical stability of monolayer  $\text{Fe}_2\text{IX}$  ( $\text{X}=\text{Cl}$  and  $\text{Br}$ ) at room temperature.

The mechanical stability of monolayer  $\text{Fe}_2\text{IX}$  ( $\text{X}=\text{Cl}$  and  $\text{Br}$ ) can be proved by elastic constants. For 2D materials, using Voigt notation, the elastic tensor with  $4mm$  point-group symmetry can be expressed as:

$$C = \begin{pmatrix} C_{11} & C_{12} & 0 \\ C_{12} & C_{11} & 0 \\ 0 & 0 & C_{66} \end{pmatrix} \quad (1)$$

The calculated  $C_{11}$ ,  $C_{12}$  and  $C_{66}$  are  $49.28 \text{ Nm}^{-1}$ ,  $16.07 \text{ Nm}^{-1}$  and  $23.68 \text{ Nm}^{-1}$  for  $\text{Fe}_2\text{ICl}$ , and  $48.53 \text{ Nm}^{-1}$ ,  $13.27 \text{ Nm}^{-1}$  and  $20.91 \text{ Nm}^{-1}$  for  $\text{Fe}_2\text{IBr}$ . The calculated elastic constants satisfy the Born criteria of mechanical stability:

$$C_{11} > 0, \quad C_{66} > 0, \quad C_{11} - C_{12} > 0 \quad (2)$$

Therefore, Janus monolayer  $\text{Fe}_2\text{IX}$  ( $\text{X}=\text{Cl}$  and  $\text{Br}$ ) is mechanically stable.

The direction-dependent mechanical properties of monolayer  $\text{Fe}_2\text{IX}$  ( $\text{X}=\text{Cl}$  and  $\text{Br}$ ) can be attained from the calculated  $C_{ij}$ . The in-plane Young's moduli  $C_{2D}(\theta)$  and Poisson's ratios  $\nu_{2D}(\theta)$  can be calculated by using the two formulas<sup>45,46</sup>:

$$C_{2D}(\theta) = \frac{C_{11}C_{22} - C_{12}^2}{C_{11}m^4 + C_{22}n^4 + (B - 2C_{12})m^2n^2} \quad (3)$$

$$\nu_{2D}(\theta) = \frac{(C_{11} + C_{22} - B)m^2n^2 - C_{12}(m^4 + n^4)}{C_{11}m^4 + C_{22}n^4 + (B - 2C_{12})m^2n^2} \quad (4)$$

where  $m = \sin(\theta)$ ,  $n = \cos(\theta)$  and  $B = (C_{11}C_{22} - C_{12}^2)/C_{66}$ . The  $\theta$  is the angle of the direction with the x direction as  $0^\circ$  and the y direction as  $90^\circ$ .

The Young's moduli  $C_{2D}(\theta)$  and Poisson's ratios  $\nu_{2D}(\theta)$  as a function of the angle  $\theta$  are shown in Figure 1. Due to the symmetric structure, both the Young's modulus and Poisson's ratios are equivalent along the (100) and (010) directions, and we only consider the angle range from  $0^\circ$  to  $90^\circ$ . The softest direction is along the (100) direction, with their Youngs moduli of  $44.04 \text{ Nm}^{-1}$  ( $\text{Fe}_2\text{ICl}$ ) and  $44.90 \text{ Nm}^{-1}$  ( $\text{Fe}_2\text{IBr}$ ). The hardest direction is along the (110) direction, with their Young's moduli of  $54.91 \text{ Nm}^{-1}$  ( $\text{Fe}_2\text{ICl}$ ) and  $49.88 \text{ Nm}^{-1}$  ( $\text{Fe}_2\text{IBr}$ ). The maximum value of Young's moduli is less than that of graphene ( $340 \text{ Nm}^{-1}$ )<sup>47</sup>, which means extraordinary flexibilities. The minima of the direction-dependent Poisson's ratios of monolayer  $\text{Fe}_2\text{IX}$  ( $\text{X}=\text{Cl}$  and  $\text{Br}$ ) is along the (110) direction (0.160 and 0.193), while the maxima is along the (100) direction (0.326 and 0.273).

#### V. TOPOLOGICAL PROPERTIES

The piezoelectric materials should be semiconductors for prohibiting current leakage. Figure 4 show the energy

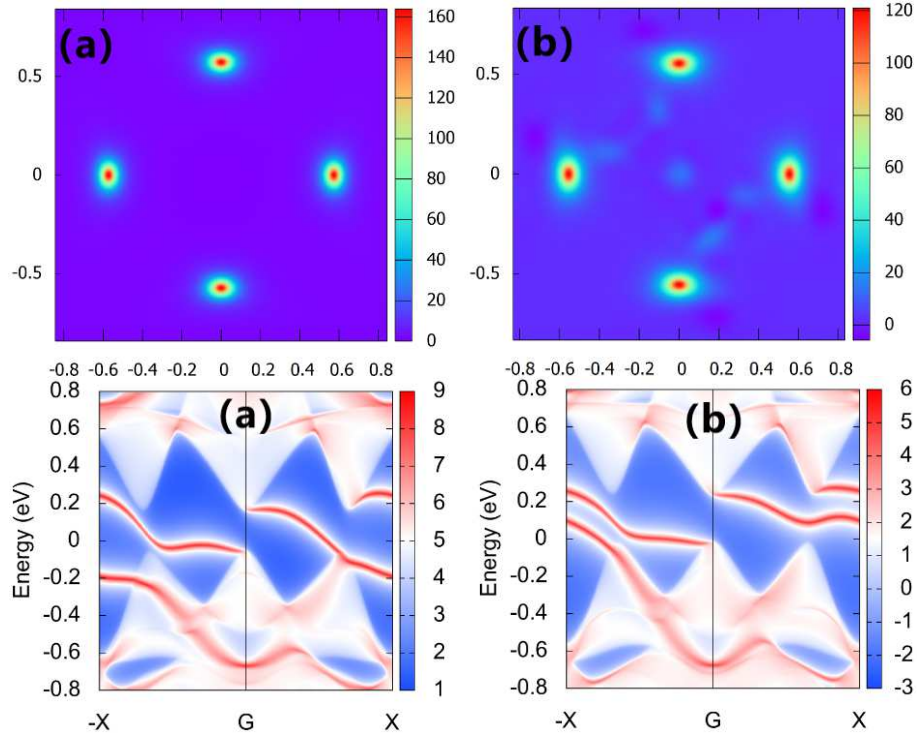


FIG. 5. (Color online) Top: the distribution of Berry curvature of  $\text{Fe}_2\text{ICl}$  (a) and  $\text{Fe}_2\text{IBr}$  (b) contributed by occupied valence bands in the momentum space. Bottom: the topological edge states of  $\text{Fe}_2\text{ICl}$  (a) and  $\text{Fe}_2\text{IBr}$  (b) calculated along the (100) direction.

band structures of monolayer  $\text{Fe}_2\text{IX}$  ( $\text{X}=\text{Cl}$  and  $\text{Br}$ ) with GGA and GGA+SOC. When the SOC is absent, monolayer  $\text{Fe}_2\text{IX}$  ( $\text{X}=\text{Cl}$  and  $\text{Br}$ ) gives a novel spin polarized state with a large-gap insulator for spin up and a gapless Dirac semimetal for spin down, namely 2D half Dirac semimetal state. Due to similar electronic properties between  $\text{Fe}_2\text{ICl}$  and  $\text{Fe}_2\text{IBr}$ , the element characters of the spin-up and spin-down bands of only  $\text{Fe}_2\text{IBr}$  monolayer using GGA are plotted in Fig.1 of electronic supplementary information (ESI), and the Fe  $d$ -orbital characters of the minority-spin bands are shown in Fig.2 of ESI. Due to the short distance between Fe atoms (about 2.65 Å), the Fe-Fe hybridization is strong for 3d orbitals. For the Fe-3d, the spin-up channel is fully occupied, while the partially occupied spin-down channel crosses the Fermi level (see Fig.1 of ESI). And then, when the magnetic moment of neighboring Fe atoms are parallelly aligned, the direct electron hopping is allowed. The strong FM kinetic exchange is in favour of FM order<sup>48</sup>. It is found that the two spin-down bands near the Fermi level are mainly contributed by  $d_{xy}$ ,  $d_{z^2}$  and  $d_{x^2-y^2}$  orbitals of Fe atom (see Fig.2 of ESI). The special electronic structures mean that these systems may be QAH insulators, when the SOC is included. In contrast to typical Dirac cones in graphene, the four Dirac cones in monolayer  $\text{Fe}_2\text{IX}$  ( $\text{X}=\text{Cl}$  and  $\text{Br}$ ) are observed. When including the SOC, the Dirac gap can be produced, and the corresponding gap is 0.223 eV for  $\text{Fe}_2\text{ICl}$  and 0.260 eV for  $\text{Fe}_2\text{IBr}$ . Similar results can be found in monolayer  $\text{Fe}_2\text{I}_2$  and lithium-

decorated iron-based superconductor materials<sup>31,49</sup>.

To verify the topologically nontrivial properties, the Chern number of monolayer  $\text{Fe}_2\text{IX}$  ( $\text{X}=\text{Cl}$  and  $\text{Br}$ ) can be calculated by integrating the Berry curvature ( $\Omega_z(k)$ ) of the occupied bands:

$$C = \frac{1}{2\pi} \int_{\text{BZ}} d^2k \Omega_z(k) \quad (5)$$

$$\Omega_z(k) = \nabla_k \times i \langle \mu_{n,k} | \nabla_k | \mu_{n,k} \rangle \quad (6)$$

where  $\mu_{n,k}$  is the lattice periodic part of the Bloch wave functions. The distributions of Berry curvature in the momentum space for  $\text{Fe}_2\text{IX}$  ( $\text{X}=\text{Cl}$  and  $\text{Br}$ ) are plotted in Figure 5. For each gapped Dirac cone, a quantized Berry phase of  $\pi$  can be attained from the valence states. The total Berry phase of  $4\pi$  is obtained due to four Dirac cones, which means a high Chern number  $C=2$ . To corroborate this finding, topological edge states along the (100) direction are calculated, which are shown in Figure 5. It is clearly seen that two chiral gapless edge modes appear within the bulk gap, which is consistent with the calculated Chern invariant. These prove that monolayer  $\text{Fe}_2\text{IX}$  ( $\text{X}=\text{Cl}$  and  $\text{Br}$ ) is still QAH insulator, which is constructed from QAH insulator  $\text{Fe}_2\text{I}_2$ <sup>31</sup>.

Next, we investigate biaxial strain effects on the QAH properties of  $\text{Fe}_2\text{IX}$  ( $\text{X}=\text{Cl}$  and  $\text{Br}$ ). Here, the  $a/a_0$  (0.94-1.06) is used to simulate the biaxial strain, in which  $a$  and

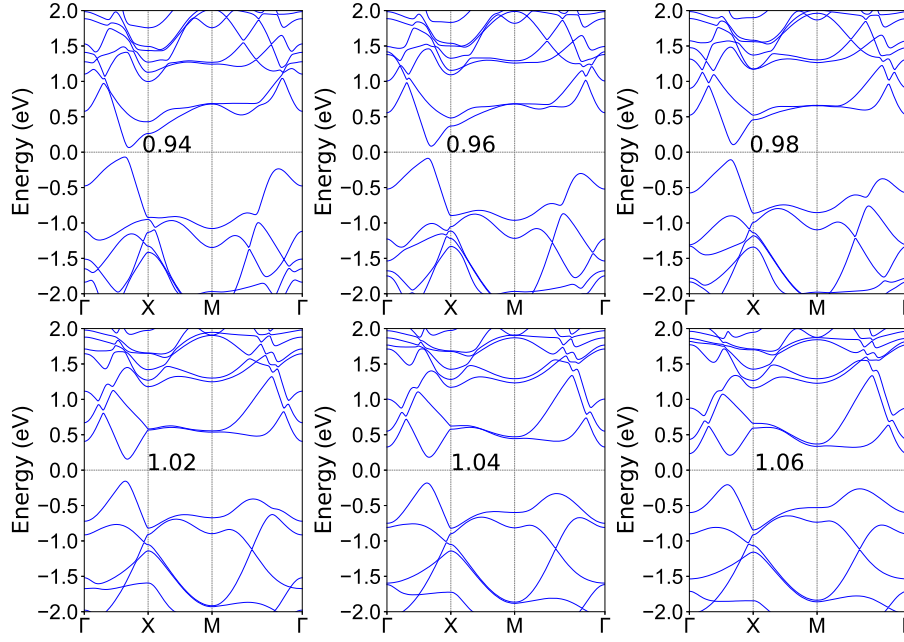


FIG. 6. (Color online) The energy band structures of  $\text{Fe}_2\text{IBr}$  monolayer using GGA+SOC with  $a/a_0$  changing from 0.94 to 1.06.

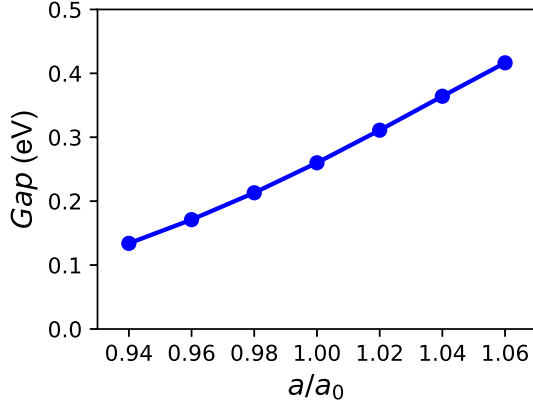


FIG. 7. (Color online) For monolayer  $\text{Fe}_2\text{IBr}$ , the gap with the application of biaxial strain (0.94 to 1.06) using GGA+SOC.

$a_0$  are the strained and unstrained lattice constants, respectively. From Figure 2, it is found that the ground states of all strained monolayers are FM in considered strain range. The energy band structures of  $\text{Fe}_2\text{IBr}$  monolayer using GGA+SOC with FM order ( $a/a_0$  from 0.94 to 1.06) are plotted in Figure 6. It is clearly seen that all considered strained monolayers are FM semiconductors. The gaps of monolayer  $\text{Fe}_2\text{IBr}$  as a function of strain are shown in Figure 7. The gap of  $\text{Fe}_2\text{IBr}$  is found to increase almost linearly with strain from 0.94 to 1.06. At 1.06 strain, the gap is up to 0.417 eV for monolayer  $\text{Fe}_2\text{IBr}$ . In considered strain range, the topological edge states of monolayer  $\text{Fe}_2\text{IBr}$  are calculated, and we show topological edge states at representative 0.94 and 1.06 strains in Figure 8. It is clearly seen that two chi-

ral topologically protected gapless edge states emerge, giving Chern number  $C=2$ . For monolayer  $\text{Fe}_2\text{ICl}$ , similar results can be found, and the strained energy band structures, gaps and topological edge states are plotted in Fig.3, Fig.4 and Fig.5 of ESI. For monolayer  $\text{Fe}_2\text{ICl}$ , the gap is up to 0.353 eV at 1.06 strain. These prove that monolayer  $\text{Fe}_2\text{IX}$  ( $X=\text{Cl}$  and  $\text{Br}$ ) possesses robust QAH states against strain.

## VI. PIEZOELECTRIC PROPERTIES

Due to  $P4/nmm$  point-group symmetry, the  $\text{Fe}_2\text{I}_2$  monolayer are centrosymmetric without piezoelectricity. The monolayer  $\text{Fe}_2\text{IX}$  ( $X=\text{Cl}$  and  $\text{Br}$ ) with  $P4mm$  point-group symmetry lacks reflectional symmetry across the  $xy$  plane, but has the reflectional symmetry across the  $xz$  or  $yz$  plane. These mean that in-plane piezoelectricity will disappear, and only out-of-plane piezoelectricity can exist. The third-rank piezoelectric stress tensor  $e_{ijk}$  and strain tensor  $d_{ijk}$  can be used to describe the piezoelectric effects of a material, which include ionic and electronic contributions. The  $e_{ijk}$  and  $d_{ijk}$  are defined as:

$$e_{ijk} = \frac{\partial P_i}{\partial \varepsilon_{jk}} = e_{ijk}^{\text{elc}} + e_{ijk}^{\text{ion}} \quad (7)$$

and

$$d_{ijk} = \frac{\partial P_i}{\partial \sigma_{jk}} = d_{ijk}^{\text{elc}} + d_{ijk}^{\text{ion}} \quad (8)$$

where  $P_i$ ,  $\varepsilon_{jk}$  and  $\sigma_{jk}$  are polarization vector, strain and stress, respectively. The  $e_{ijk}^{\text{elc}}/d_{ijk}^{\text{elc}}$  only considers electronic contributions, namely clamped-ion piezoelectric

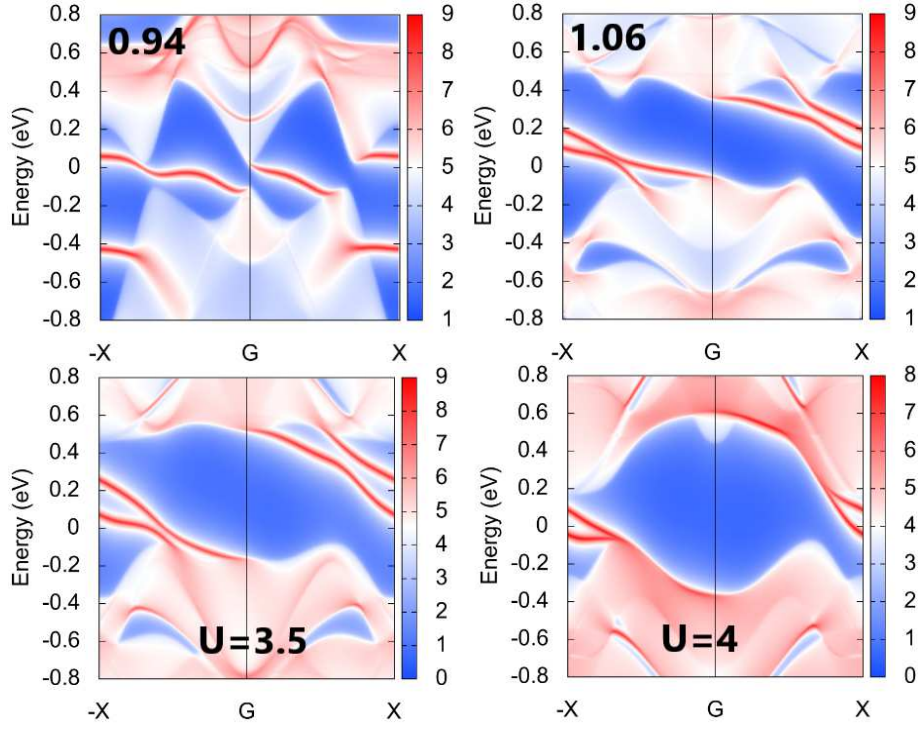


FIG. 8. (Color online) Top: the topological edge states of Fe<sub>2</sub>IBr calculated along the (100) direction at 0.94 and 1.06 strains. Bottom: the topological edge states of Fe<sub>2</sub>IBr calculated along the (100) direction at  $U=3.5$  eV and  $U=4.0$  eV.

coefficients. The  $e_{ijk}/d_{ijk}$  is from the sum of ionic and electronic contributions, namely relax-ion piezoelectric coefficients as a realistic result. The  $e_{ijk}$  can be related with  $d_{ijk}$  by elastic tensor  $C_{mnjk}$ :

$$e_{ijk} = \frac{\partial P_i}{\partial \varepsilon_{jk}} = \frac{\partial P_i}{\partial \sigma_{mn}} \cdot \frac{\partial \sigma_{mn}}{\partial \varepsilon_{jk}} = d_{imn} C_{mnjk} \quad (9)$$

For 2D materials, only the in-plane strain and stress ( $\varepsilon_{jk} = \sigma_{ij} = 0$  for  $i=3$  or  $j=3$ ) are taken into account<sup>6–11</sup>. By using Voigt notation, the piezoelectric stress and strain tensors of monolayer Fe<sub>2</sub>IX (X=Cl and Br) can be reduced into:

$$e = \begin{pmatrix} 0 & 0 & 0 \\ 0 & 0 & 0 \\ e_{31} & e_{31} & 0 \end{pmatrix} \quad (10)$$

$$d = \begin{pmatrix} 0 & 0 & 0 \\ 0 & 0 & 0 \\ d_{31} & d_{31} & 0 \end{pmatrix} \quad (11)$$

With a applied uniaxial or biaxial in-plane strain, only vertical piezoelectric polarization ( $e_{31}/d_{31} \neq 0$ ) can be produced. The  $e_{31}$  can be calculated by DFPT, and the  $d_{31}$  can be derived by Equation 9, Equation 10 and Equation 11.

$$d_{31} = \frac{e_{31}}{C_{11} + C_{12}} \quad (12)$$

TABLE II. For Janus monolayer Fe<sub>2</sub>IX (X=Cl and Br), the elastic constants  $C_{ij}$  in  $\text{Nm}^{-1}$ , the piezoelectric stress coefficients  $e_{31}$  in  $10^{-10}$  C/m, the piezoelectric strain coefficients  $d_{31}$  in pm/V, MAE in  $\mu\text{eV}/\text{Fe}$ , easy axis (EA) and normalized exchange parameter  $J$ .

Name	$C_{11}$	$C_{12}$	$C_{66}$	$e_{31}$	$d_{31}$	MAE	EA	$J$
Fe <sub>2</sub> ICl	49.28	16.07	23.68	0.305	0.467	39	$c$	57.0
Fe <sub>2</sub> IBr	48.53	13.27	20.91	0.237	0.384	318	$c$	53.5

The primitive cell is used to calculate the  $e_{31}$  of Janus monolayer Fe<sub>2</sub>IX (X=Cl and Br). The calculated  $e_{31}$  is  $0.305 \times 10^{-10}$  C/m with ionic part  $0.027 \times 10^{-10}$  C/m and electronic part  $0.278 \times 10^{-10}$  C/m for Fe<sub>2</sub>ICl, and  $0.237 \times 10^{-10}$  C/m with ionic contribution  $0.087 \times 10^{-10}$  C/m and electronic contribution  $0.150 \times 10^{-10}$  C/m for Fe<sub>2</sub>IBr. Calculated results show that the electronic and ionic polarizations have the same signs, and the electronic contribution is larger than the ionic part for Janus monolayer Fe<sub>2</sub>IX (X=Cl and Br). According to Equation 12, the  $d_{31}$  can be attained, and the calculated value is 0.467 pm/V for Fe<sub>2</sub>ICl, and 0.384 pm/V for Fe<sub>2</sub>IBr. To be compatible with the nowadays bottom/top gate technologies, a large out-of-plane piezoelectric  $d_{31}$  is highly desired for 2D materials. The  $d_{31}$  of Janus monolayer Fe<sub>2</sub>IX (X=Cl and Br) is higher than ones of many 2D materials, like Janus TMD monolayers (0.03 pm/V)<sup>6</sup>, functionalized h-BN (0.13 pm/V)<sup>50</sup> and kalium decorated graphene (0.3 pm/V)<sup>51</sup>, and is comparable with ones of the oxygen

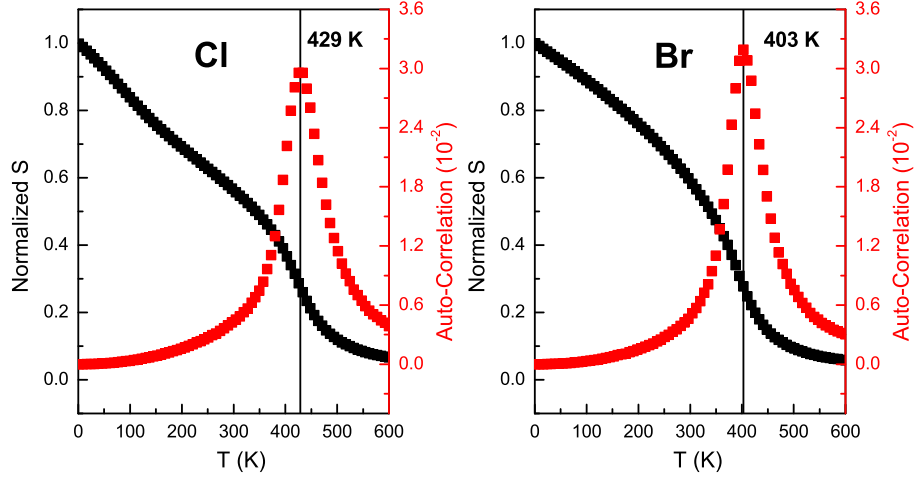


FIG. 9. (Color online) The normalized magnetic moment (S) and auto-correlation of Janus monolayer  $\text{Fe}_2\text{IX}$  ( $\text{X}=\text{Cl}$  and  $\text{Br}$ ) as a function of temperature.

functionalized MXenes (0.40-0.78 pm/V)<sup>15</sup>, Janus group-III materials (0.46 pm/V)<sup>52</sup>, Janus  $\text{BiTeI}/\text{SbTeI}$  monolayer (0.37-0.66 pm/V)<sup>53</sup> and  $\alpha\text{-In}_2\text{Se}_3$  (0.415 pm/V)<sup>54</sup>.

## VII. CURIE TEMPERATURE

Curie temperatures ( $T_C$ ) is a very important parameter for the practical application of monolayer  $\text{Fe}_2\text{IX}$  ( $\text{X}=\text{Cl}$  and  $\text{Br}$ ). By using Heisenberg model, the MC simulations are carried out to estimate the  $T_C$  of monolayer  $\text{Fe}_2\text{IX}$  ( $\text{X}=\text{Cl}$  and  $\text{Br}$ ). The spin Heisenberg Hamiltonian is defined as:

$$H = -J \sum_{i,j} S_i \cdot S_j - A \sum_i (S_i^z)^2 \quad (13)$$

in which  $J$ ,  $S$  and  $A$  are the nearest neighbor exchange parameter, the spin vector of each atom and anisotropy energy parameter, respectively. Using the energy difference between AFM and FM and normalized  $S$  ( $|S|=1$ ), the magnetic coupling parameters are calculated as  $J=(E_{\text{AFM}}-E_{\text{FM}})/8$ . The calculated  $J$  value is 57.0 meV for  $\text{Fe}_2\text{ICl}$ , and 53.5 meV for  $\text{Fe}_2\text{IBr}$ .

The magnetic anisotropy energy (MAE) plays a very important role to determine the thermal stability of magnetic ordering, which mainly originates from the SOC interaction. The GGA+SOC calculations are used to obtain relative stabilities along the (100) and (001) directions. The related data are summarized in Table II. It is found that the easy axes of these monolayers are along the out-of-plane (001) direction. A  $40 \times 40$  supercell and  $10^7$  loops are adopted to carry out the MC simulation. The normalized magnetic moment and auto-correlation of monolayer  $\text{Fe}_2\text{IX}$  ( $\text{X}=\text{Cl}$  and  $\text{Br}$ ) as a function of temperature are plotted in Figure 9. It can be seen that  $T_C$  is as high as 429 K/403 K for  $\text{Fe}_2\text{ICl}/\text{Fe}_2\text{IBr}$ , which is significantly higher than that of

previously reported many 2D FM semiconductors, like  $\text{CrI}_3$  monolayer (about 45 K)<sup>26</sup>,  $\text{CrOCl}$  monolayer (about 160 K)<sup>55</sup> and  $\text{Cr}_2\text{Ge}_2\text{Te}_6$  monolayer (about 20 K)<sup>56</sup>. The  $T_C$  for monolayer  $\text{Fe}_2\text{ICl}/\text{Fe}_2\text{IBr}$  is very close to one of  $\text{Fe}_2\text{I}_2$  monolayer<sup>31</sup>. Considering the large nontrivial band gap and out-of-plane piezoelectric polarizations combined with the high  $T_C$ , monolayer  $\text{Fe}_2\text{IX}$  ( $\text{X}=\text{Cl}$  and  $\text{Br}$ ) would provide a promising platform for exploring the PQAHE effect at room temperature.

## VIII. DISCUSSION AND CONCLUSION

To understand the relationship between electronic correlation and nontrivial band topology, the electronic structures of monolayer  $\text{Fe}_2\text{IX}$  ( $\text{X}=\text{Cl}$  and  $\text{Br}$ ) are calculated by GGA+SOC with  $U$  from 0.0 eV to 4.0 eV. Some representative energy bands of monolayer  $\text{Fe}_2\text{IX}$  ( $\text{X}=\text{Cl}$  and  $\text{Br}$ ) are plotted in Fig.6 and Fig.7 of ESI, and their gaps as a function of  $U$  (0.0 to 4.0 eV) are shown in Figure 10. With increasing  $U$ , it is clearly seen that the gap increases firstly, and then decreases. At  $U=0.0$  eV, the gap is 4 meV for  $\text{Fe}_2\text{ICl}$ , and 27 meV for  $\text{Fe}_2\text{IBr}$ . At about  $U=3.5$  eV, their gaps reach maximums, and 604 meV for  $\text{Fe}_2\text{ICl}$  and 537 meV for  $\text{Fe}_2\text{IBr}$ . At  $U=4$  eV, their gaps become small, which is because the conduction band minimum (CBM)/valence band maximum (VBM) changes from one point along  $\Gamma$ -X line to M point/one point along  $\Gamma$ -M line. In considered  $U$  range, the topological edge states of monolayer  $\text{Fe}_2\text{IX}$  ( $\text{X}=\text{Cl}$  and  $\text{Br}$ ) are calculated. We show topological edge states of  $\text{Fe}_2\text{IBr}$  at representative  $U=3.5$  and 4 eV in Figure 8, and in Fig.8 of ESI for  $\text{Fe}_2\text{ICl}$ . It is clearly seen that two chiral topologically protected gapless edge states emerge, which means that the Chern number  $C=2$ . These show that monolayer  $\text{Fe}_2\text{IX}$  ( $\text{X}=\text{Cl}$  and  $\text{Br}$ ) possesses robust QAHE states against electronic correlation. Finally, the energy difference between AFM and FM states as a function of

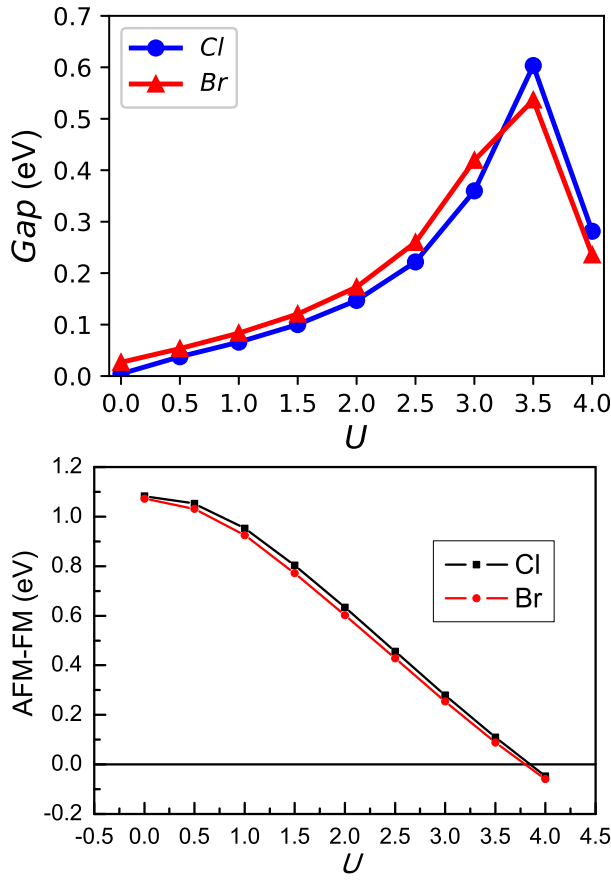


FIG. 10. (Color online) For monolayer  $\text{Fe}_2\text{IX}$  ( $\text{X}=\text{Cl}$  and  $\text{Br}$ ), Top: the gap as a function of  $U$  (0.0 to 4.0 eV) using GGA+SOC. Bottom: the energy difference between AFM and FM states as a function of  $U$  using GGA.

$U$  for monolayer  $\text{Fe}_2\text{IX}$  ( $\text{X}=\text{Cl}$  and  $\text{Br}$ ) are plotted in

Figure 10. It is found that the ground state of monolayer  $\text{Fe}_2\text{IX}$  ( $\text{X}=\text{Cl}$  and  $\text{Br}$ ) becomes AFM, when the  $U$  is larger than about 3.75 eV.

In summary, the intriguing 2D PQAIs  $\text{Fe}_2\text{IX}$  ( $\text{X}=\text{Cl}$  and  $\text{Br}$ ) are predicted by the reliable first-principle calculations. Monolayer  $\text{Fe}_2\text{IX}$  ( $\text{X}=\text{Cl}$  and  $\text{Br}$ ) exhibits excellent dynamic, mechanical and thermal stabilities, and possesses out-of-plane magnetic anisotropy and high Curie temperature. The nontrivial topology of  $\text{Fe}_2\text{IX}$  ( $\text{X}=\text{Cl}$  and  $\text{Br}$ ), identified with Chern number  $C=2$  and chiral edge states, has a nontrivial band gap of more than 200 meV. The calculated out-of-plane  $d_{31}$  is higher than or comparable with ones of other 2D known materials, which is highly desirable for ultrathin piezoelectric devices. It is proved that the emergence of robust QAH states in monolayer  $\text{Fe}_2\text{IX}$  ( $\text{X}=\text{Cl}$  and  $\text{Br}$ ) is robust against strain and electronic correlation. Our predicted room-temperature PQAIs are of crucial importance to fundamental research and to future development of electronics, piezoelectronics and spintronics, and these findings open new opportunities to realize novel practical quantum applications.

#### Conflicts of interest

There are no conflicts to declare.

#### ACKNOWLEDGMENTS

This work is supported by Natural Science Basis Research Plan in Shaanxi Province of China (2021JM-456). We are grateful to the Advanced Analysis and Computation Center of China University of Mining and Technology (CUMT) for the award of CPU hours and WIEN2k/VASP software to accomplish this work.

- <sup>1</sup> P. Lin, C. Pan and Z. L. Wang, *Materials Today Nano* **4**, 17 (2018).
- <sup>2</sup> M. Dai, Z. Wang, F. Wang, Y. Qiu, J. Zhang, C. Y. Xu, T. Zhai, W. Cao, Y. Fu, D. Jia, Y. Zhou, and P. A. Hu, *Nano Lett.* **19**, 5416 (2019).
- <sup>3</sup> W. Wu, L. Wang, Y. Li, F. Zhang, L. Lin, S. Niu, D. Chenet, X. Zhang, Y. Hao, T. F. Heinz, J. Hone and Z. L. Wang, *Nature* **514**, 470 (2014).
- <sup>4</sup> A. Y. Lu, H. Zhu, J. Xiao, C. P. Chuu, Y. Han, M. H. Chiu, C. C. Cheng, C. W. Yang, K. H. Wei, Y. Yang, Y. Wang, D. Sokaras, D. Nordlund, P. Yang, D. A. Muller, M. Y. Chou, X. Zhang and L. J. Li, *Nat. Nanotechnol.* **12**, 744 (2017).
- <sup>5</sup> H. Zhu, Y. Wang, J. Xiao, M. Liu, S. Xiong, Z. J. Wong, Z. Ye, Y. Ye, X. Yin and X. Zhang, *Nat. Nanotechnol.* **10**, 151 (2015).
- <sup>6</sup> L. Dong, J. Lou and V. B. Shenoy, *ACS Nano*, **11**, 8242 (2017).
- <sup>7</sup> R. X. Fei, W. B. Li, J. Li and L. Yang, *Appl. Phys. Lett.* **107**, 173104 (2015).

- <sup>8</sup> M. N. Blonsky, H. L. Zhuang, A. K. Singh and R. G. Hennig, *ACS Nano*, **9**, 9885 (2015).
- <sup>9</sup> S. D. Guo, Y. T. Zhu, W. Q. Mu and W. C. Ren, *EPL* **132**, 57002 (2020).
- <sup>10</sup> W. B. Li and J. Li, *Nano Res.* **8**, 3796 (2015).
- <sup>11</sup> Dimple, N. Jena, A. Rawat, R. Ahammed, M. K. Mohanta and A. D. Sarkar, *J. Mater. Chem. A* **6**, 24885 (2018).
- <sup>12</sup> N. Jena, Dimple, S. D. Behere and A. D. Sarkar, *J. Phys. Chem. C* **121**, 9181 (2017).
- <sup>13</sup> M. T. Ong and E. J. Reed, *ACS Nano* **6**, 1387 (2012).
- <sup>14</sup> A. A. M. Noor, H. J. Kim and Y. H. Shin, *Phys. Chem. Chem. Phys.* **16**, 6575 (2014).
- <sup>15</sup> J. Tan, Y. H. Wang, Z. T. Wang, X. J. He, Y. L. Liu, B. Wanga, M. I. Katsnelson and S. J. Yuan, *Nano Energy* **65**, 104058 (2019).
- <sup>16</sup> J. H. Yang, A. P. Wang, S. Z. Zhang, J. Liu, Z. C. Zhong and L. Chen, *Phys. Chem. Chem. Phys.*, **21**, 132 (2019).
- <sup>17</sup> S. D. Guo, W. Q. Mu, Y. T. Zhu and X. Q. Chen, *Phys. Chem. Chem. Phys.* **22**, 28359 (2020).
- <sup>18</sup> S. D. Guo, X. S. Guo, X. X. Cai, W. Q. Mu and W. C.

- Ren, arXiv:2103.15141 (2021).
- <sup>19</sup> G. Song, D. S. Li, H. F. Zhou et al., *Appl. Phys. Lett.* **118**, 123102 (2021).
  - <sup>20</sup> S. D. Guo, W. Q. Mu, Y. T. Zhu, S. Q. Wang and G. Z. Wang, *J. Mater. Chem. C* **9**, 5460 (2021).
  - <sup>21</sup> S. D. Guo, Y. T. Zhu, W. Q. Mu and X. Q. Chen, arXiv:2103.03456 (2021).
  - <sup>22</sup> Y. Ma, Y. Dai, M. Guo, C. Niu, Y. Zhu and B. Huang, *ACS Nano*, **6**, 1695 (2012).
  - <sup>23</sup> C. Gong, L. Li, Z. Li, H. Ji, A. Stern, Y. Xia, T. Cao, W. Bao, C. Wang, Y. Wang, Z. Q. Qiu, R. J. Cava, S. G. Louie, J. Xia and X. Zhang, *Nature* **546**, 265 (2017).
  - <sup>24</sup> M. Khazaei, M. Arai, T. Sasaki, C. Y. Chung, N. S. Venkataramanan, M. Estili, Y. Sakka and Y. Kawazoe, *Adv. Funct. Mater.* **23**, 2185 (2013).
  - <sup>25</sup> Y. Guo, H. Deng, X. Sun, X. Li, J. Zhao, J. Wu, W. Chu, S. Zhang, H. Pan, X. Zheng, X. Wu, C. Jin, C. Wu and Y. Xie, *Adv. Mater.* **29**, 1700715 (2017).
  - <sup>26</sup> B. Huang, G. Clark, E. Navarro-Moratalla, D. R. Klein, R. Cheng, K. L. Seyler, D. Zhong, E. Schmidgall, M. A. McGuire, D. H. Cobden, W. Yao, D. Xiao, P. Jarillo-Herrero and X. Xu, *Nature* **546**, 270 (2017).
  - <sup>27</sup> G. Bhattacharyya, I. Choudhuri, P. Bhauriyal, P. Garg and B. Pathak, *Nanoscale* **10**, 22280 (2018).
  - <sup>28</sup> W. B. Zhang, Q. Qu, P. Zhu and C. H. Lam, : *J. Mater. Chem. C* **3**, 12457 (2015).
  - <sup>29</sup> C. Z. Chang, J. S. Zhang, X. Feng et al., *Science* **340**, 167 (2013).
  - <sup>30</sup> J. G. Checkelsky, J. T. Ye, Y. Onose et al., *Nat. Phys.* **8**, 729 (2012).
  - <sup>31</sup> Q. L. Sun, Y. D. Ma and N. Kioussis, *Mater. Horiz.* **7**, 2071 (2020).
  - <sup>32</sup> A. Y. Lu, H. Y. Zhu, J. Xiao et al., *Nature Nanotechnology* **12**, 744 (2017).
  - <sup>33</sup> P. Hohenberg and W. Kohn, *Phys. Rev.* **136**, B864 (1964); W. Kohn and L. J. Sham, *Phys. Rev.* **140**, A1133 (1965).
  - <sup>34</sup> G. Kresse, *J. Non-Cryst. Solids* **193**, 222 (1995).
  - <sup>35</sup> G. Kresse and J. Furthmüller, *Comput. Mater. Sci.* **6**, 15 (1996).
  - <sup>36</sup> G. Kresse and D. Joubert, *Phys. Rev. B* **59**, 1758 (1999).
  - <sup>37</sup> J. P. Perdew, K. Burke and M. Ernzerhof, *Phys. Rev. Lett.* **77**, 3865 (1996).
  - <sup>38</sup> V. I. Anisimov, F. Aryasetiawan and A. I. Lichtenstein, *J. Phys. Condens. Mat.* **9**, 767 (1997).
  - <sup>39</sup> J. Heyd, G. E. Scuseria and M. Ernzerhof, *J. Chem. Phys.* **118**, 8207 (2003).
  - <sup>40</sup> X. Wu, D. Vanderbilt and D. R. Hamann, *Phys. Rev. B* **72**, 035105 (2005).
  - <sup>41</sup> A. Togo, F. Oba, and I. Tanaka, *Phys. Rev. B* **78**, 134106 (2008).
  - <sup>42</sup> Q. Wu, S. Zhang, H. F. Song, M. Troyer and A. A. Soluyanov, *Comput. Phys. Commun.* **224**, 405 (2018).
  - <sup>43</sup> A. A. Mostofia, J. R. Yatesb, G. Pizzif, Y.-S. Lee, I. Souzad, D. Vanderbilt and N. Marzarif, *Comput. Phys. Commun.* **185**, 2309 (2014).
  - <sup>44</sup> L. Liu, X. Ren, J. H. Xie, B. Cheng, W. K. Liu, T. Y. An, H. W. Qin and J. F. Hu, *Appl. Surf. Sci.* **480**, 300 (2019).
  - <sup>45</sup> E. Cadelano and L. Colombo, *Phys. Rev. B* **85**, 245434 (2012).
  - <sup>46</sup> E. Cadelano, P. L. Palla, S. Giordano, and L. Colombo, *Phys. Rev. B* **82**, 235414 (2010).
  - <sup>47</sup> C. Lee, X. Wei, J. W. Kysar, and J. Hone, *Science* **321**, 385 (2008).
  - <sup>48</sup> M. Eremin and Y. V. Rakitin, *J. Phys. C* **14**, 247 (1981).
  - <sup>49</sup> Y. Li, J. H. Li, Y. Li et al., *Phys. Rev. Lett.* **125**, 086401 (2020).
  - <sup>50</sup> A. A. M. Noor, H. J. Kim and Y. H. Shin, *Phys. Chem. Chem. Phys.* **16**, 6575 (2014).
  - <sup>51</sup> M. T. Ong and E. J. Reed, *ACS Nano* **6**, 1387 (2012).
  - <sup>52</sup> Y. Guo, S. Zhou, Y. Z. Bai, and J. J. Zhao, *Appl. Phys. Lett.* **110**, 163102 (2017).
  - <sup>53</sup> S. D. Guo, X. S. Guo, Z. Y. Liu and Y. N. Quan, *J. Appl. Phys.* **127**, 064302 (2020).
  - <sup>54</sup> L. Hu and X.R. Huang, *RSC Adv.* **7**, 55034 (2017).
  - <sup>55</sup> N. Miao, B. Xu, L. Zhu, J. Zhou and Z. Sun, *J. Am. Chem. Soc.* **140**, 2417 (2018).
  - <sup>56</sup> C. Gong, L. Li, Z. Li, H. Ji, A. Stern, Y. Xia, T. Cao, W. Bao, C. Wang, Y. Wang, Z. Q. Qiu, R. J. Cava, S. G. Louie, J. Xia and X. Zhang, *Nature* **546**, 265 (2017).